

# Shellular Metamaterial Design via Compact Electric Potential Parametrization

CHANG LIU and BOHAN WANG, National University of Singapore, Singapore

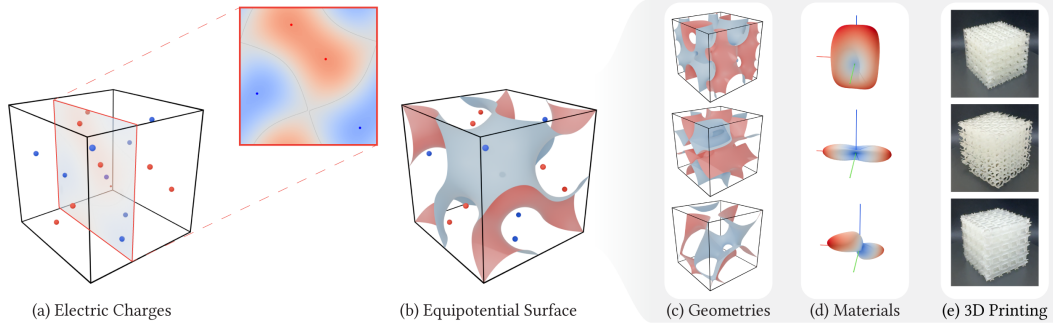


Fig. 1. **Design of shellular metamaterials.** Our structures are represented by an implicit function parameterized by a few dozen electric charges (a). By arranging these charges, we obtain a broad set of geometrically diverse structures (b,c). These structures also exhibit a wide range of properties (c) and remain feasible for fabrication in practical applications (e).

We introduce a compact yet highly expressive design space for shellular metamaterials. By employing only a few dozen degrees of freedom, this design space represents geometries ranging from simple planar configurations to complex triply periodic minimal surfaces. Coupled with this representation, we develop an efficient GPU-based homogenization pipeline that evaluates the structure in under 20 ms and computes the corresponding effective elastic tensor in near-real-time (0.5 s). The high speed of this evaluation facilitates an exhaustive exploration of the design space and supports an inverse-design scheme that tailors the shellular structure to specific macroscopic target property. Structures derived through this approach exhibit not only geometric diversity but also a wide spectrum of mechanical responses, covering a broad range of material properties. Moreover, they achieve up to 91.86% of theoretical upper bounds, a level of performance comparable to state-of-the-art shellular structures with low solid volume. Finally, our prototypes, fabricated via additive manufacturing, confirm the practical manufacturability of these designs, underscoring their potential for real-world engineering applications.

CCS Concepts: • **Computing methodologies** → **Modeling methodologies**; **Shape modeling**; • **Applied computing** → *Computer-aided design*.

Additional Key Words and Phrases: cellular metamaterials, microstructures, shellular, triply periodic minimal surfaces (TPMS), optimization, CUDA

## ACM Reference Format:

Chang Liu and Bohan Wang. 2025. Shellular Metamaterial Design via Compact Electric Potential Parametrization. 1, 1 (November 2025), 10 pages. <https://doi.org/10.1145/nnnnnnn.nnnnnnn>

Authors' Contact Information: Chang Liu, [willliu@nus.edu.sg](mailto:willliu@nus.edu.sg); Bohan Wang, [bh.wang@nus.edu.com](mailto:bh.wang@nus.edu.com), National University of Singapore, Singapore.

Permission to make digital or hard copies of all or part of this work for personal or classroom use is granted without fee provided that copies are not made or distributed for profit or commercial advantage and that copies bear this notice and the full citation on the first page. Copyrights for components of this work owned by others than the author(s) must be honored. Abstracting with credit is permitted. To copy otherwise, or republish, to post on servers or to redistribute to lists, requires prior specific permission and/or a fee. Request permissions from [permissions@acm.org](mailto:permissions@acm.org).

© 2025 Copyright held by the owner/author(s). Publication rights licensed to ACM. ACM XXXX-XXXX/2025/11-ART <https://doi.org/10.1145/nnnnnnn.nnnnnnn>

## 1 Introduction

Metamaterials have long been of interest because they exhibit material properties that differ from those of their constituent materials. Rather than relying solely on chemical composition, these properties arise predominantly from the structural arrangement of cellular architectures [Babae et al. 2013; Fang et al. 2018; Mao et al. 2020]. Within the family of 3D metamaterials, shellular structures stand out due to their minimal volumetric occupation and advantageous geometric features. These characteristics enable significant material savings while preserving structural integrity. In fact, in some instances, shellular structures can outperform other architecture types [Torquato et al. 2002]. As a result, shellular structure designs have emerged as key elements in numerous applications, including 3D-printed infill patterns, heat exchanger interfaces, and reconfigurable thin-shell systems.

Despite numerous advances in the field, designing shellular metamaterials remains challenging. Although several automated design approaches have been introduced, they typically impose restrictive design spaces. Many studies concentrate on a limited range of structures; for example, Panetta et al. [2015] explored only truss-based architectures, leaving other types of structures largely unexplored. For shellular structures, while existing approaches can generate them, these methods often involve solving intricate optimization or simulation problems to represent a narrow range of shellular structures, leading to significant computational complexity and limited property diversity [Hsieh et al. 2019; Xu et al. 2023a; Zhang and Liu 2025]. Conversely, procedure-based or voxel-based methods seek to develop highly flexible design representations that can encode a wide variety of metamaterial geometries. However, the procedural generator do not support both efficient structure generation and automatic structural design [Makatura et al. 2023], whereas voxel-based representations use excessively large design spaces [Eschenauer and Olhoff 2001], inheriting the drawbacks of conventional topology optimization.

To address these limitations, we propose a novel design space that is both computationally efficient and sufficiently expressive to capture a broad range of shellular structures. Our approach simultaneously achieves geometric diversity and tunable material properties, demonstrating great potential for shellular metamaterial design. Additionally, we introduce a highly efficient, GPU-based computation and optimization framework, enabling rapid structure evaluation. Furthermore, we develop a design and optimization method that, given user-defined objectives, can automatically identify the desired structure. Collectively, these contributions significantly expand the design possibilities for shellular metamaterials beyond current constraints.

Finally, we validate the proposed approach through comprehensive experiments. First, our evaluations are performed efficiently, requiring on average less than 20 ms to generate a shellular structure. Furthermore, our representation demonstrate diversity and high performance across a broad range of material properties, including Young’s modulus, bulk modulus, shear modulus, and off-diagonal components of the elastic tensor. Our randomly generated shellular structures cover a large span of material properties. Moreover, our representation accommodates geometries ranging from simple planar shapes to more intricate shellular forms, such as Triply Periodic Minimal Surfaces (TPMS). Additionally, we also illustrate the capability of our framework to design materials according to specific objectives, including maximizing bulk modulus, maximizing shear stiffness, or achieving a targeted Young’s modulus. Several of our designs reach up to 91.86% of the theoretical upper bound. Finally, we fabricate multiple examples to demonstrate that our proposed designs are fully manufacturable.

## 2 Related Work

### 2.1 Cellular Metamaterials

Architected (mechanical) metamaterials are artificially engineered materials whose effective mechanical properties primarily originate from the geometry of their unit-cell architecture rather than from their constituent composition [Bertoldi et al. 2017; Kadic et al. 2013; Lu et al. 2022]. In this paper, we focus on *shellular* metamaterials, a particular type of mechanical metamaterial that usually fits within a *cubic* unit cell and is composed of a *homogeneous* elastic material forming thin shells. These shells can constitute either a two-dimensional manifold surface embedded in three-dimensional space [Nguyen et al. 2016] or a non-manifold or non-smooth surface [Spadoni et al. 2014]. A prominent example within this class is the family of TPMS, which have been extensively studied and deployed in various applications [Han and Che 2018]. TPMS structures, characterized by zero mean curvature across their surfaces, exhibit reduced stress concentration and are well suited to additive manufacturing. Beyond “true” TPMS, there are TPMS-like structures that share similar qualities [Hu et al. 2020; Jiang et al. 2023; Xu et al. 2023b]. Our proposed design space is capable of incorporating a broad range of these TPMS-like structures. There are also other smooth surface, such as the one with spindoidal topologies [Hsieh et al. 2019], which is solution of Cahn-Hilliard equation.

### 2.2 Design Space

An intuitive design space for shellular structures is to use techniques from geometric shape modeling. For instance, one may construct a thin shell deformation basis using either geometric energies (e.g., Biharmonic energy [Wang et al. 2015]) or polynomial functions (e.g., NURBS [Piegl and Tiller 2012]). These control handles form the design space of the surface. However, such approaches require a predefined mesh template, which is difficult to create for a given property requirement. Moreover, the topology of the template is fixed during optimization. Finally, these bases are generic and not specifically designed for metamaterials, which often demand specialized boundary conditions, such as periodic constraints.

Another widely adopted strategy defines the surface via an Eulerian field, with the signed distance function as a representative example [Osher et al. 2003]. However, the voxel values are the design space, making it prohibitively large to represent thin shells. Numerous studies have sought to reduce this design space via neural networks or model-reduction techniques [Park et al. 2019], but these methods typically require a priori shellular metamaterial datasets that are difficult to acquire. Hsieh et al. [2019] use the solution of the Cahn-Hilliard equation to define the shell structures, but it takes six hours for solving the equation [Kumar et al. 2020].

An alternative is to represent thin shells by specifying boundary loops [Makatura et al. 2023; Palmer et al. 2022; Xu et al. 2023b]. Nonetheless, constructing patches from these loops requires solving multiple optimization problems (typically taking dozens of seconds or minutes), which makes large-scale data acquisition cumbersome. In addition to performance constraints, the modeling of the loops itself is a complex problem. To simplify the problem, these methods often define them within a fundamental volume and then replicate the resulting patches across the entire unit cell, leading to restricted symmetry of the structure.

### 2.3 Homogenization

Different types of solids have led to various homogenization approaches. Schumacher et al. [2018] introduced a macroscale equivalent thin-shell model to derive parameters for mesoscale thin shells, while Yuan et al. [2024] proposed a novel volumetric homogenization method specifically targeting knitwear. Additionally, Chen and Otaduy presented a high-order RBF interpolation technique in polar coordinates to address thin-shell homogenization [Chan-Lock and Otaduy 2024]. Although our work also focuses on thin shells, we regard our building blocks as three-dimensional unit cells rather than patches, distinguishing our approach from prior studies. Recently, data-driven surrogate models have emerged, including physics-informed neural networks equipped with spectral normalization, which strictly enforce Voigt–Reuss bounds and provide rapid yet physically consistent tensor predictions [Keshav et al. 2025].

We use a Finite-Element-based homogenization scheme [Geers et al. 2010], whereby linear elasticity is solved on a representative volume element (RVE). We apply a uniform strain to the RVE for homogenization [Panetta et al. 2015; Zhang et al. 2023]. Other formulations such as energy-based formulation that imposes unit test strains directly on the boundaries of the base cell also exist [Xia and Breitkopf 2015]. According to Hashin [1983], this energy-based

scheme is equivalent to the standard asymptotic homogenization for predicting effective material properties [Guedes and Kikuchi 1990].

### 3 Design Space

#### 3.1 Surface Parameterization

A shellular structure is often represented by a Signed Distance Field (SDF). It is an implicit function in which the value zero identifies the surface. Our objective is to parameterize the SDF in a low-dimensional space. Inspired by electrostatics, we observe that an electric charge generates a potential field that depends on distance. Moreover, when there is an equal number of positive and negative charges, the resulting potential field closely resembles a SDF (see the inset). In such a configuration, the surface appears at the location where the electric potential is zero. As a point moves farther from this zero-potential surface, the magnitude of the potential grows in a manner analogous to the SDF.

Based on this observation, instead of defining a surface by an SDF, we represent the shellular structure through an electric potential field governed by a finite number of electric charges. The resulting surface is an equipotential surface. Hence, the design space for the shellular structure is characterized only by the positions and values of these charges, leading to a substantial reduction in the dimensionality of the control parameters. The implicit function is written as

$$F(x, y, z) = \iiint \frac{\rho(\xi, \eta, \zeta) d\xi d\eta d\zeta}{\sqrt{(x - \xi)^2 + (y - \eta)^2 + (z - \zeta)^2}}, \quad (1)$$

where

$$\rho(x, y, z) = \sum_{j=1}^N q_j \delta(x - x_j, y - y_j, z - z_j) \quad (2)$$

is the charge distribution in 3D space,  $\delta(\cdot)$  is the Kronecker delta function,  $(x_j, y_j, z_j)$  is the position of the  $j$ -th charge, and  $q_j$  is its value. For a shellular metamaterial, we impose periodic boundary conditions on the unit cell. Consequently, the electric charge distribution becomes a periodic function:

$$\rho(x, y, z) = \sum_{j=1}^N q_j \sum_{\substack{m, n, p = -\infty \\ m, n, p \in \mathbb{Z}}}^{\infty} \delta(x - m - x_j, y - n - y_j, z - p - z_j). \quad (3)$$

Barnes [1990] showed that, under these conditions in a unit cubic cell with period equal to 1, there is a closed-form expression for the

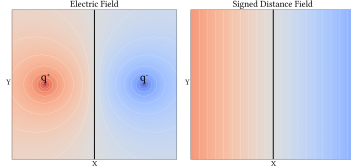


Fig. 2. **The electric charge potential behaves similarly to the signed distance function.** Only two charges are necessary to represent a plane (black solid vertical line).

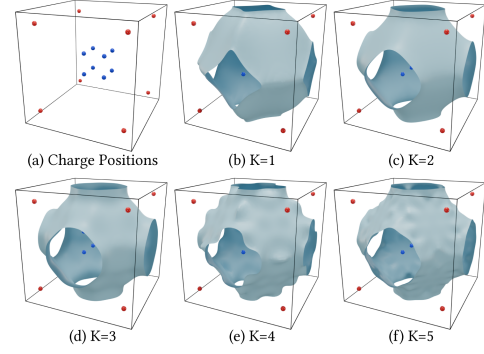


Fig. 3. **Different numbers of bases lead to distinct surface.** Here, we assume that  $\alpha_{hkl} = 1$ .

resulting implicit function derived via a Fourier transform:

$$F(x, y, z) = \frac{8}{\pi} \sum_{j=1}^N q_j \sum_{\substack{h, k, l = 0 \\ h, k, l \in \mathbb{Z}}}^{\infty} w_{hkl} B_{hkl}(x, y, z, x_j, y_j, z_j), \quad (4)$$

$$B_{hkl}(x, y, z, x_j, y_j, z_j) = \frac{\cos(2\pi h(x - x_j)) \cos(2\pi k(y - y_j)) \cos(2\pi l(z - z_j))}{h^2 + k^2 + l^2}, \quad (5)$$

where  $w_{hkl} = 1/2$  if exactly one of  $(h, k, l)$  is zero and  $w_{hkl} = 1/4$  if two of the indices are zero.

Since the above series is infinite, it cannot be directly utilized to construct a finite-dimensional design space. Based on extensive experiments, we truncate  $F$  to a finite series with charges  $q_j \in \{+1, -1\}$ , enforcing an equal number of positive and negative charges. We also introduce weights  $\alpha_{hkl}$  for  $h, k, l \leq K$  and let  $B_{000}(\cdot) = 0$ , leading to:

$$F(x, y, z) = \sum_{j=1}^N \sum_{\substack{h, k, l = 0 \\ h, k, l \in \mathbb{Z}}}^K \alpha_{hkl} w_{hkl} B_{hkl}(x, y, z, x_j, y_j, z_j) - \sum_{j=N+1}^{2N} \sum_{\substack{h, k, l = 0 \\ h, k, l \in \mathbb{Z}}}^K \alpha_{hkl} w_{hkl} B_{hkl}(x, y, z, x_j, y_j, z_j). \quad (6)$$

In this formulation, the arrangement of charge positions and the weighting factors  $\alpha_{hkl}$  collectively determines the surface geometry. Figure 3 presents an example with 16 charges at different values of  $K$ , assuming  $\alpha_{hkl} = 1$ . As  $K$  increases, the surface exhibits sharper features and appears smoother overall, although it also becomes bumpier on a finer scale. By tuning  $\alpha_{hkl}$ , one can further refine the surface details. As demonstrated in Sec. 5.2, even a relatively small number of charges and basis functions can produce a broad range of surfaces. Barnes [1990] also showed that a special case of our formulation can represent several well-known TPMS structures. Moreover, because the dimension of this design space is low, the design process can be carried out efficiently using various optimization methods, including first-order and gradient-free approaches.

### 3.2 Structure Symmetry

Building upon the existing design space, one can choose to impose structural symmetry by defining a *Fundamental Bounding Volume* (FBV), as other methods did. Rather than specifying charges throughout the entire unit cell, charges are assigned only within this FBV and then mirrored to span the full unit cell. This approach not only ensures structural symmetry but also reduces the dimensionality of the design space. For example, although Figure 3 presents an example with 16 charges, these charges are mirrored throughout the unit cell from only two charges located in a cubic FBV, yielding a symmetric final structure. Such structural symmetry often results in specific material properties, for instance, orthotropic behavior. In the Supplementary Material, we prove that symmetric charge configurations necessarily produce symmetric structures. Typical FBVs include a region covering one-eighth of the unit cell or a tetrahedral domain, as discussed in [Panetta et al. 2015]. In this paper, we use both of them as the FBVs.

## 4 Efficient Homogenization

### 4.1 Energy-based Homogenization in 3D

To determine the effective material properties of the shellular structure, we employ a homogenization procedure for computing the effective elastic tensor. Specifically, we adopt an energy-based approach from the engineering community [Xia and Breitkopf 2015] and adapt it to the 3D setting with efficient GPU implementation. As shown below, by suitably simplifying the governing equations, a concise linear formulation can be obtained.

Consider a cubic unit cell serving as a RVE, which is discretized into a set of voxel-based finite elements  $e \in Y$ , where  $Y$  denotes the set of all elements. The homogenized elastic tensor  $C^H$  is computed via

$$C_{ijkl}^H = \frac{1}{|Y|} \sum_{e \in Y} (\mathbf{u}_e^{eij})^T K_e \mathbf{u}_e^{ekl}, \quad (7)$$

where  $\mathbf{u}_e^{eij}$  is the displacement of element  $e$  when the periodic domain is subjected to a unit test strain  $\varepsilon^{ij} = \mathbf{e}_i \otimes \mathbf{e}_j$ . The vectors  $\mathbf{e}_i \in \mathbb{R}^3, i = 1 \dots 3$ , are the standard basis vectors in  $\mathbb{R}^3$ . We obtain  $\mathbf{u}_e^{eij}$  by solving the static equilibrium of linear elasticity under periodic boundary conditions (PBCs)

$$\mathbf{K}\mathbf{u} = \mathbf{f}, \quad \text{st. } \mathbf{u} \text{ is periodic,}$$

where  $\mathbf{K}$  is the tangent stiffness matrix.

Under the assumption of periodicity, the displacement field  $u$  of the base cell subjected to an arbitrary strain tensor  $\varepsilon$  can be decomposed into  $u = \varepsilon y + u^*$ , where  $y$  is the local cartesian coordinate at the microscale, and  $u^*$  is a periodic fluctuation. Let  $u^{k+}$  and  $u^{k-}$  be displacements at a pair of opposite faces of the unit cell in the  $k$ -th direction ( $k = 1, 2, 3$ ). Then, the periodic boundary condition is expressed as

$$u^{k+} - u^{k-} = \varepsilon(y^{k+} - y^{k-}) = \varepsilon \Delta y^k = \varepsilon \mathbf{e}_k, \quad (8)$$

where the fluctuation terms cancel out, and  $\Delta y^k$  identifies with the  $k$ -th basis vector  $\mathbf{e}_k$  due to the unit length of the cell. This relation will serve as an explicit periodic constraint applying to each cell boundary node when solving for  $\mathbf{u}^{ij}$ . Since the same procedure is

applied to each test strain, we temporarily omit the superscript  $\varepsilon^{ij}$  in subsequent derivations for brevity.

To simplify the solving, we partition the node displacements  $\mathbf{u}$  into eight groups:  $\mathbf{u} = [(\mathbf{u}^i)^T]^T, i = 1 \dots 8$ . Here,  $\mathbf{u}^1$  corresponds to nodes with prescribed displacements  $\bar{\mathbf{u}}$ , typically corner nodes used to eliminate rigid body motion. One corner is fixed at the origin, and the other corner displacements are set according to Eq. (8). The vector  $\mathbf{u}^2$  gathers the displacements of interior nodes not on the boundary. The vectors  $\mathbf{u}^3$  and  $\mathbf{u}^4$  represent displacements of boundary face nodes that do not lie on edges or corners. They are of the same size, satisfying  $\mathbf{u}^4 = \mathbf{u}^3 + \mathbf{w}^0$ , where  $\mathbf{w}^0$  is a constant determined by  $\varepsilon \mathbf{e}_k$  in (8). Similarly,  $\mathbf{u}^i (i = 5, 6, 7, 8)$  denotes displacements of boundary edge nodes (excluding corner vertices), where all of them are of equal size and satisfy  $\mathbf{u}^i = \mathbf{u}^5 + \mathbf{w}^{i-4} (i = 6, 7, 8)$ . The vector  $\mathbf{w}^i$  is once again derived from Eq. (8). Accordingly, the linear elasticity equation becomes

$$\mathbf{K}_{ij} \mathbf{u}^j = \mathbf{f}^i, \quad i = 1 \dots 8,$$

$$\mathbf{u}^1 = \bar{\mathbf{u}},$$

$$\mathbf{u}^4 = \mathbf{u}^3 + \mathbf{w}^0,$$

$$\mathbf{u}^k = \mathbf{u}^5 + \mathbf{w}^{k-4}, \quad k = 6, 7, 8$$

For interior nodes, the net force vanishes, i.e.,  $\mathbf{f}^2 = 0$ . For nodes with prescribed displacements,  $\mathbf{u}^1$  is given directly. Due to PBCs, the forces on opposite faces appear with opposite signs, so  $\mathbf{f}^3 + \mathbf{f}^4 = 0$ . Likewise,  $\mathbf{f}^5 + \mathbf{f}^6 + \mathbf{f}^7 + \mathbf{f}^8 = 0$  for edges. Utilizing the displacement relations among these vectors, one can reduce the equation into three block matrices:

$$\begin{bmatrix} \mathbf{K}_{22} & \mathbf{Z}_{2324} & \mathbf{Z}_{2528} \\ \mathbf{Z}_{3234} & \mathbf{Z}_{3344} & \mathbf{Z}_{3548} \\ \mathbf{Z}_{5282} & \mathbf{Z}_{5384} & \mathbf{Z}_{5588} \end{bmatrix} \begin{bmatrix} \mathbf{u}^2 \\ \mathbf{u}^3 \\ \mathbf{u}^5 \end{bmatrix} = - \begin{bmatrix} \mathbf{K}_{21} \\ \mathbf{Z}_{3141} \\ \mathbf{Z}_{5181} \end{bmatrix} \bar{\mathbf{u}} - \begin{bmatrix} \mathbf{K}_{24} \\ \mathbf{Z}_{3444} \\ \mathbf{Z}_{5484} \end{bmatrix} \mathbf{w}^0 - \begin{bmatrix} \mathbf{K}_{26} \\ \mathbf{Z}_{3646} \\ \mathbf{Z}_{5686} \end{bmatrix} \mathbf{w}^1 - \begin{bmatrix} \mathbf{K}_{27} \\ \mathbf{Z}_{3747} \\ \mathbf{Z}_{5787} \end{bmatrix} \mathbf{w}^2 - \begin{bmatrix} \mathbf{K}_{28} \\ \mathbf{Z}_{3848} \\ \mathbf{Z}_{5888} \end{bmatrix} \mathbf{w}^3, \quad (9)$$

where  $\mathbf{Z}_{ijkl} = \sum_{p=i}^k \sum_{q=j}^l \mathbf{K}_{pq}$ . For simplicity, we rewrite Eq. (9) as  $\mathbf{A}\bar{\mathbf{u}} = -\mathbf{B}\bar{\mathbf{u}} - \sum_{i=0}^3 \mathbf{C}_i \mathbf{w}^i$ . The final solution follows  $\mathbf{u} = \mathbf{S}\bar{\mathbf{u}} + \mathbf{t}$ , where  $\mathbf{S}$  and  $\mathbf{t}$  are constants determined by the aforementioned PBC relations. Thus, the solution for the displacement field under a particular test strain  $\varepsilon^{ij}$  can be expressed as

$$\mathbf{u}^{\varepsilon^{ij}} = -\mathbf{S}\mathbf{A}^{-1} \left( \mathbf{B}\bar{\mathbf{u}}^{\varepsilon^{ij}} + \sum_{k=0}^3 \mathbf{C}_k \mathbf{w}^{k,\varepsilon^{ij}} \right) + \mathbf{t}^{\varepsilon^{ij}}. \quad (10)$$

With this expression, we determine the displacement field and then the effective elastic tensor can be computed directly from them using Eq. (7).

### 4.2 Homogenization of the Shellular Structure

To compute the homogenized elastic tensor of the shellular structure, we first embed the shellular surface into the unit cell voxel mesh and then apply our voxel-based homogenization framework. The tangent stiffness matrix of each voxel element, denoted by  $K_e$ , is then given by

$$K_e = \beta_e K_0 = h(F(x_e, y_e, z_e)) K_0, \quad (11)$$

**ALGORITHM 1:** Shellular Structure Homogenization

**Input:** Particle positions  $(x_j, y_j, z_j)$ ,  $j = 1 \dots 2N$ ; weights  $\alpha_{hkl}, h, k, l = 0 \dots K$

**Output:** Effective elastic tensor  $C^H$

Compute field  $F(x, y, z)$  from  $(x_j, y_j, z_j)$  and  $\alpha_{hkl}$  ▶ Eq. (6)  
 Build voxel mesh ▶ Sec. 4.2  
 Identify node pairs on the periodic boundary ▶ Sec. 4.2  
 Build matrix  $A, S$  ▶ Eq. (9) and Sec. 4.3  
 Solve linear system and compute  $\mathbf{u}$  ▶ Eq. (10) and Sec. 4.3  
 Compute elastic tensor  $C^H$  ▶ Eq. (7) and Sec. 4.3  
**return**  $C^H$

where  $\beta_e$  is the ratio that mimics how much volume each voxel is occupied by the shell structure, and  $h(\cdot)$  is a customized step function defined as

$$h(v) = 1 + \frac{v_0}{2} - \frac{v_0}{(1 + e^{-kv^2})}, \quad (12)$$

and  $p_e = (x_e, y_e, z_e)$  is the center of each voxel. The matrix  $K_0$  is the (constant) tangent stiffness matrix for a single voxel element, which is identical for all voxels. In the step function  $h(\cdot)$ , the parameter  $k$  controls how thin the shellular surface is, while  $v_0$  avoids ill-conditioned linear systems.

However, using the full voxel mesh for the entire domain would leave most voxels empty, causing significant performance issues. Therefore, instead of employing the full mesh, we construct a voxel mesh that tightly encloses the surface. As a result, only about 9.5% of voxels are required, leading to consid-

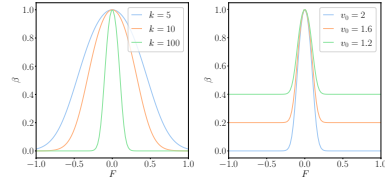


Fig. 4. Plot of  $h(\cdot)$  as a function of  $k$  and  $v_0$ . A larger value of  $k$  sharpens the function, resulting in a thinner shellular structure. Meanwhile, the parameter  $v_0$  helps alleviate numerical issues by preventing  $K_e$  from reaching zero.

erable improvements in the linear solver performance. We first identify all voxels intersecting the surface, then expand the mesh based on the surface thickness using a Breadth-First-Search (BFS)-style algorithm. Next, we enforce periodicity on the mesh boundaries by adding missing voxels. After building this reduced voxel mesh, we compute the periodic pairs of boundary nodes. Alg. 1 illustrates the entire workflow.

### 4.3 GPU Implementation

To implement Eq. (7), (10) efficiently on a GPU, we divide the solution process into four primary steps: (1) assemble the sparse matrices  $S$  and  $A$ , (2) assemble the right-hand side (RHS), (3) solve the resulting linear system, and (4) compute  $C^H$ . The sparse matrix  $A$  is positive-definite. We employ a direct solver rather than an iterative approach, as our numerical experiments reveal that a GPU-based conjugate gradient (CG) solver – despite forgoing explicit construction of  $A$  – is  $1.91\times$  slower than a GPU-accelerated direct solver in our setup. Hence, we explicitly store  $A$  in a compressed format and use a direct solver.

Method	$t_{\text{field}}$	$t_{\text{mesh}}$	$t_{\text{PBC}}$	$t_{A,S}$	$t_{\text{RHS}}$	$t_{\text{solve}}$	$t_C$	$t_{\text{fwd}}$
CPU	151.38	2.5	40.12	3976.62	5.62	2216.80	13.2	6406.24
Ours	13.78	1.31	1.02	19.45	8.18	399.78	1.64	445.16

Table 1. **Our GPU-based method achieves a  $15\times$  speedup compared with a multithreaded CPU implementation that explicitly computes the sparse matrices.** We measure the computational time of each step in the pipeline. The symbols are defined in Table 2.

In the first step, we pre-allocate a GPU global array of size  $|Y|\times 24\times 24$  to store the row-column-value triplets required for constructing the matrix  $A$  in Coordinate List (COO) format, as each element can contribute up to  $24\times 24$  triplets. Then, a CUDA thread is launched for every element and write its own memory segment starting at  $e\times 24\times 24$ . It first decomposes the local stiffness matrix  $K_e$  into  $3\times 3$  node blocks, each corresponding to a pair of nodes. Then, if this pair of nodes are involved in  $A$ , the block is transformed into row-column-value triplets and write to the memory; or, we write a zero triplet. Because each CUDA thread access its own global memory segment, it avoids any memory access contention. Next, a GPU-based parallel reduction (`reduce_by_key_with_sum`) merges these triplets into a new array without duplicated row-column indices, that is the COO-format of  $A$ . Finally, we convert it into Compressed Sparse Row (CSR) format for the direct solver. As shown in Table 1, our matrix assembling is  $204\times$  faster than a CPU multi-threaded implementation which explicitly disassembles the  $K$  matrix into blocks and re-assembles them to form  $A$ .

In step two, we build the RHS vector in parallel by launching a CUDA thread for each element. Again, we disassemble  $K_e$  into  $3\times 3$  blocks, load the relevant vector portion (from  $\mathbf{u}^f$  or  $\mathbf{w}^k$ ), perform the  $3\times 3$  matrix-vector product, and add the local result to the global RHS using an `atomicAdd` operation. Because our matrices  $B$  and  $C_k$  are implicitly stored, our RHS computation is slightly slower than the CPU counter parts, as shown in Table 1.

Finally, we perform the symbolic and numeric factorization of  $A$  using cuDSS [NVIDIA 2024]. Since  $A$  is independent of the test strains, we solve the RHS for each of the six independent unit test strains simultaneously. The GPU-based solver offers a  $5.5\times$  speedup over the CPU direct solver (Table 1). Once the displacements are determined, we perform a final GPU-based reduction to compute the homogenized elastic tensor according to Eq. (7). Overall, our proposed method is  $14.4\times$  faster than the CPU energy-based implementation<sup>1</sup>, thereby achieving near-real-time performance. Furthermore, our results closely match those of the reference implementation<sup>1</sup>, with an average relative error of 1.7%.

<sup>1</sup><https://github.com/MeshFEM/MeshFEM>

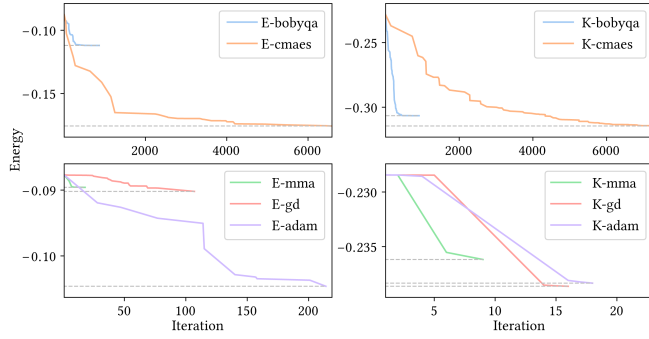


Fig. 5. **Energy plot of each optimization method.** We compare multiple gradient-free and gradient-based optimization methods in terms of their effectiveness at lowering the energy. Our findings indicate that the gradient-free methods outperform the gradient-based method in both problems.

#### 4.4 Inverse Design Based on Homogenization

To design the shellular structure, we consider the following optimization problem:

$$\arg \min_{p_m, \alpha_{hkl}} \mathcal{E}(C^H),$$

$$\text{where } C_{ijkl}^H = \frac{1}{|Y|} \sum_{e \in Y} (\mathbf{u}_e^{ij})^T \beta_e K_0 \mathbf{u}_e^{kl},$$

$$\mathbf{u}^{e^{ij}} = -\mathbf{S}(\mathbf{A}(\beta))^{-1} \left( \mathbf{B}(\beta) \bar{\mathbf{u}}^{e^{ij}} + \sum_{k=0}^3 C_k(\beta) \mathbf{w}^{k, e^{ij}} \right) + \mathbf{t}^{e^{ij}},$$

$$\beta_e = h(F(p_e; p_m, \alpha_{hkl})),$$

$$i, j = 1, \dots, 6, \quad m = 1, \dots, 2N, \quad h, k, l = 0, \dots, K,$$

$p_m = (x_m, y_m, z_m)$  denotes the position of charge  $m$ , and  $\mathcal{E}(\cdot)$  is a function of  $C^H$  tailored to the specific design objective. Next, we outline how this optimization problem is solved efficiently.

Initially, we employed a first-order gradient-based method, taking advantage of the fact that the effective elastic tensor  $C^H$  is fully differentiable with respect to the charge positions  $p_j = (x_j, y_j, z_j)$  and the weights  $\alpha_{hkl}$ . We derived the corresponding gradients (see Suppl.), implemented them on a GPU, and applied several optimization algorithms, including the MMA algorithm [Svanberg 2002], gradient descent [Ruder 2016], and the Adam optimizer [Kingma and Ba 2014]. Two common objectives are tested: maximizing the average Young’s modulus and maximizing the bulk modulus. The results, shown in Fig. 5, indicate that these methods successfully reduce the energy but only to a limited extent. We also test an inexact gradient by omitting the derivative of  $C^H$  with respect to  $\mathbf{u}$ , following a practice in topology optimization [Xia and Breitkopf 2015], but find that it exhibits similar convergence behavior, likely due to the noisy energy landscape in our design space.

Consequently, we turn to gradient-free optimizers. Our design space has relatively low dimensionality, namely  $((K + 1)^3 - 1 + 6N)$ , and our energy evaluations run quickly. We therefore test BOBYQA [Powell et al. 2009] and CMA-ES [Arnold and Hansen 2010] on the same objectives. Both achieve lower energy values than the gradient-based approach and do so more efficiently; one iteration of the gradient-based method costs approximately  $20\times$  a single energy evaluation. Among the tested methods, CMA-ES yields the lowest final value but takes around  $7\times$  longer to converge than BOBYQA,

a reasonable trade-off given its more global search capability compared to the local search of BOBYQA. For all subsequent designs, we therefore use CMA-ES.

## 5 Results

We comprehensively evaluate our method in terms of performance, structural diversity, structural property, and practical applications. All experiments are conducted on a desktop machine equipped with an RTX 5090 GPU, a 32-core Threadripper 3970X CPU, and 256 GB of memory, running Ubuntu 24.04 with CUDA 12.9. The homogenization framework, encompassing both forward computation and inverse design, is fully implemented in C++ with CUDA. We employ cuDSS [NVIDIA 2024] as the linear solver, while cusparse and cublas handle the linear algebra routines. Our approach relies on only two parameters: the number of charges, denoted  $2N$ , and the number of basis functions,  $K$ . Although we vary  $2N$  according to particular applications,  $K$  is fixed to 2 for all the examples presented.

### 5.1 Computational Cost

In Table 2, we present the forward and backward computation times at various resolutions and input sizes. The results indicate that, for resolutions of 64 or below, our implementation can achieve near-real-time evaluation (approximately 0.5 s), with solving the linear system being the main bottleneck. In contrast, the backward phase is substantially less efficient, thereby motivating the use of gradient-free optimization. Note that we show the time cost of an exact gradient computation as opposed to semi-implicit-style inexact gradient like [Zhang et al. 2023], which requires much more number of linear solve per iteration. Although the number of charges has a minimal effect on the forward computation, it significantly affects the backward computation due to the expanded number of degrees of freedom. Due to the limitation of the size of GPU memory, all subsequent calculations in this work are conducted at a resolution of 64. Moreover, generating these structures is highly efficient, taking only about 14 ms, which indicates strong potential for applications requiring rapid structure generation.

### 5.2 Random Structure Generation

We randomly generate 1,000 structures using 8 and 16 charges for a cubic FBV, 4 and 8 charges for a tetrahedron FBV, and 64 and 128 charges without an FBV (i.e., no symmetry), resulting in total 6,000 structures. We then evaluate the diversity in the Young’s moduli along the x-, y-, and z-axes ( $E_k$ ), the bulk modulus ( $K_{\text{eff}}$ ), the shear modulus ( $G_{\text{eff}}$ ), the universal anisotropic index (UAI) [Ranganathan and Ostoja-Starzewski 2008], and the sum of the absolute values of the off-block-diagonal entries. For the bulk and shear moduli, we use Hill’s approximation [Hill 1952] by taking the average of the Voigt upper bound and the Reuss lower bound. The Young’s modulus is computed by  $E_k = 1/((C^H)^{-1})_{kk}$ . Additional details are provided in the Supplementary Materials.

We compare our results with the theoretical Hashin–Shtrikman (HS) upper bounds for both the bulk modulus and the shear modulus [Hashin and Shtrikman 1963]. For the Young’s modulus, we use the simple Voigt upper bound  $vE$  [Voigt 1910], where  $v$  is the

$r$	$n_q$	$n_e$	$t_{\text{field}}$	$t_{\text{mesh}}$	$t_{\text{PBC}}$	$t_{\text{A,S}}$	$t_{\text{RHS}}$	$t_{\text{sol}}$	$t_{\text{C}}$	$t_{\text{fwd}}$	$t_{\text{bkRHS}}$	$t_{\text{bkSol}}$	$t_{\text{bkC}}$	$t_{\text{bk}}$	GPU Mem
32	8	6,180.62	2.36	0.65	0.18	3.49	2.63	129.42	0.52	139.26	458.66	1,913.83	100.35	2,472.84	1.72GB
64	8	23,601.94	13.78	1.31	1.02	19.45	8.18	399.78	1.64	445.16	2,210.14	6,637.48	273.28	9,120.90	2.25GB
64	64	20,361.91	13.54	1.25	1.08	17.27	6.93	318.84	1.45	360.38	10,149.28	26,098.31	1,144.46	37,392.05	6.32GB
64	128	20,862.56	14.79	1.35	1.07	16.70	7.14	336.79	1.42	379.25	9,509.96	25,552.93	1,086.94	36,149.83	11.48GB
128	8	451,960.0	104.65	32.96	7.71	471.85	95.43	11,800.45	29.98	12,543.03	47,780.06	89,033.39	1,917.93	138,731.38	25.05GB

Table 2. **Time cost analysis of each stage in our method.** The quantity  $t_{\text{field}}$  denotes the time to compute the electric potential field, and  $t_{\text{mesh}}$  corresponds to the time spent identifying voxels and computing  $\beta_e$ . Next,  $t_{\text{PBC}}$  represents the time to identify periodic boundary pairs of nodes,  $t_{\text{A,S}}$  is the time to form the sparse matrices,  $t_{\text{RHS}}$  refers to the time to construct the right-hand side (RHS),  $t_{\text{solve}}$  is the time to solve the linear equation,  $t_{\text{C}}$  is the time to compute the final elastic tensor, and  $t_{\text{fwd}}$  is the total time cost for the forward phase. During the backward phase,  $t_{\text{bkRHS}}$  is the time required to compute derivatives of the summation with respect to the charge position and weights,  $t_{\text{bkSol}}$  is the time to compute the derivative of  $\mathbf{u}$  with respect to the charge position and weights, and  $t_{\text{bkC}}$  is the time to compute the final derivative. The total backward-phase cost is  $t_{\text{bk}}$ , and “GPU Mem” indicates the peak GPU memory usage. All values are reported in milliseconds.

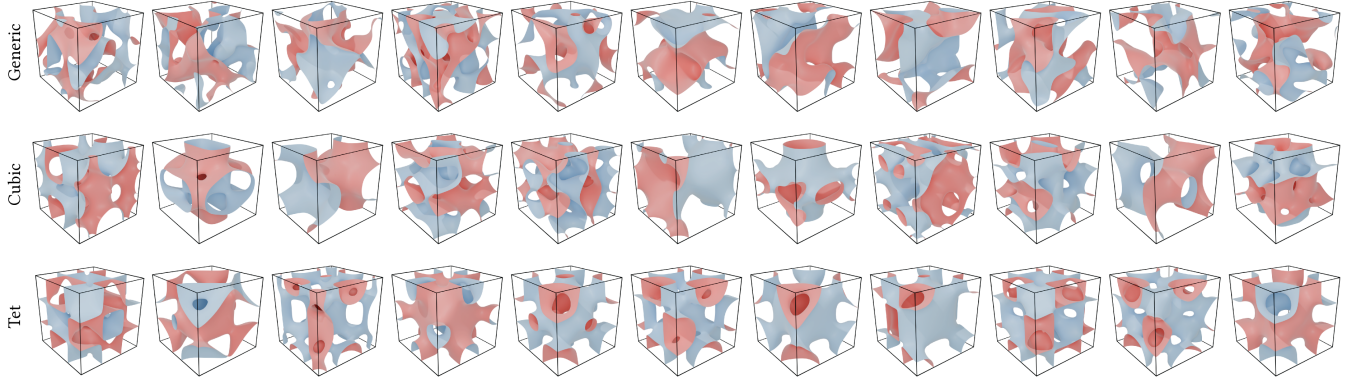


Fig. 6. **Our design space can cover a large set of structures with diverse geometry.** Here we show three type of structures, structures constructed without symmetric, structures built from cubic FBV, and structure built from tetrahedron FBV.

volume ratio and  $E$  is the base Young’s modulus, owing to the primarily anisotropic nature of our material. Nevertheless, the bulk modulus remains unaffected by this anisotropy. A selection of these structures is illustrated in Figure 6, highlighting the diversity of the generated geometries. Furthermore, Figure 7 demonstrates that these structures exhibit a wide range of material properties in all evaluated aspects, indicating significant potential for diverse and practical applications.

### 5.3 Representing Existing Structures

Our approach can also capture TPMS and other shellular structures. To achieve this, we first compute a set of TPMS configurations using an accurate method [Makatura et al. 2023] or based on trigonometric functions. We then fit our representation to match these geometries by solving the following optimization problem:

$$\arg \min_{p_m, \alpha_{hkl}} \sum_i F^2(\bar{p}_i; p_m, \alpha_{hkl}) - \lambda \sum_i \tanh(sF^2(\bar{p}_i; p_m, \alpha_{hkl})), \quad (13)$$

where  $\bar{p}_i$  denotes a randomly sampled point on the target surface,  $\bar{q}_i$  is a randomly sampled point at a distance  $d$  (we use  $d \geq 0.05$ ) from the target surface,  $s$  is the inverse of absolute maximum of  $F$  in each iteration (used to normalize  $F$ ), and  $\lambda$  is a hyperparameter. The first term ensures that our shellular representation passes through the points  $\bar{p}_i$ . The second term enforces separation from  $\bar{q}_i$  by making  $F$  nonzero. We use the hyperbolic tangent function  $\tanh$  because we do not want  $F$  to grow arbitrarily large; it only needs to be sufficiently

away from zero. We solve the optimization using Adam [Kingma and Ba 2014].

Using this approach, we fit a considerable number of surfaces, including 50 TPMS and 3 planar surfaces, thereby demonstrating our method’s ability to capture complex geometries. A subset of results are presented in Figure 8. To assess the accuracy of our reconstructions, we compare the reconstructed surfaces with the reference geometries by computing both the average distance and the Hausdorff distance, as reported in Figure 8. Our findings show that the resulting surfaces are closely matched with the ground truth, both visually and quantitatively. In addition, the properties of all fit surfaces are illustrated in Figure 7.

### 5.4 Optimal Structure Search

We evaluate our inverse-design pipeline on six distinct optimization problems:

- (1) **Largest Young’s modulus in the x-direction.** The objective is defined as  $\mathcal{E}(C^H) = -E_k/V$ , where  $V = \frac{1}{V_{\text{all}}} \sum_e \beta_e$ .
- (2) **Largest Young’s modulus in an isotropic material.** The objective is defined as  $\mathcal{E}(C^H) = -E_{\text{eff}}/V + \gamma \mathcal{E}_{\text{iso}}(C^H)$ .
- (3) **Largest bulk modulus.** The objective is  $\mathcal{E}(C^H) = -K_{\text{eff}}/V$ .
- (4) **Largest shear modulus.** The objective is  $\mathcal{E}(C^H) = -G_{\text{eff}}/V$ .
- (5) **Largest off-diagonal components.** Here, the objective is  $\mathcal{E}(C^H) = -\sum_{i=1}^3 \sum_{j=3}^6 |C_{ij}^H|$ .

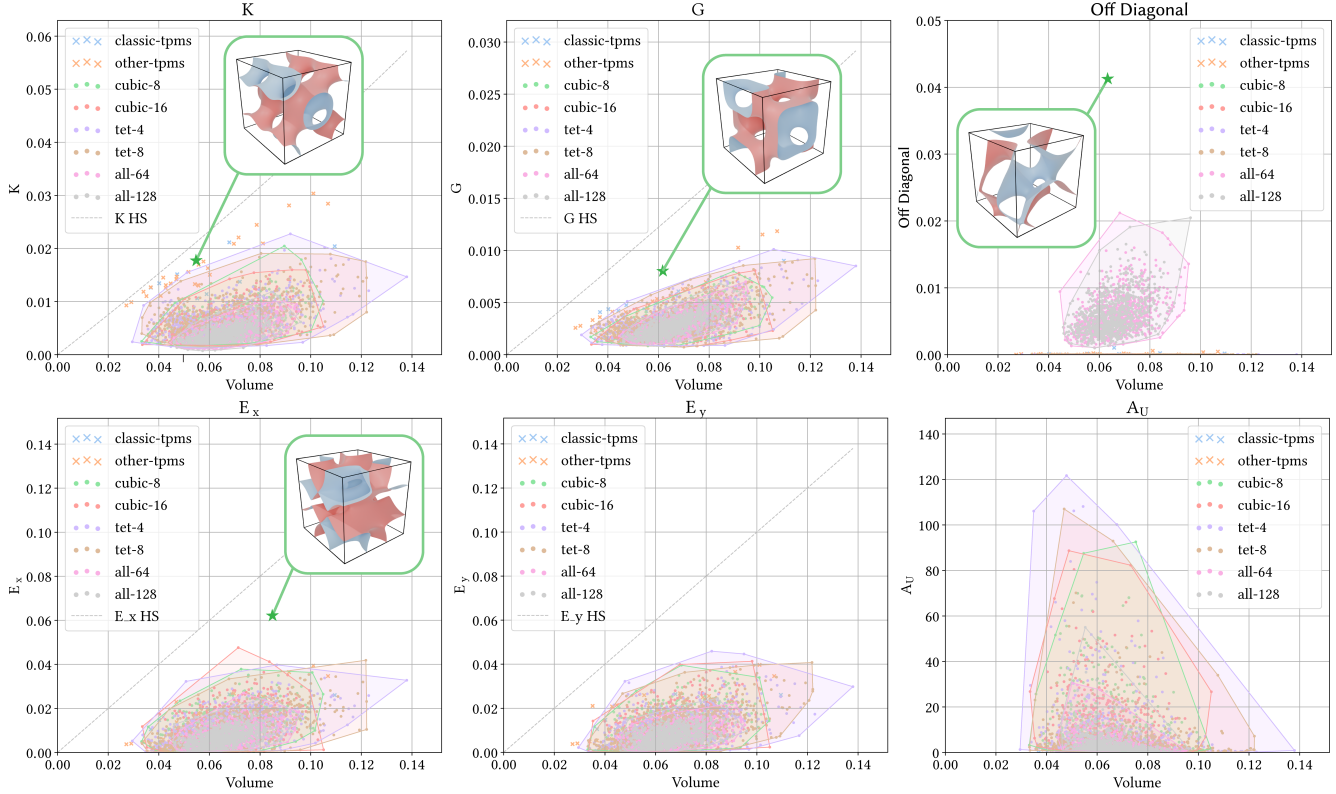


Fig. 7. **Our design space spans a wide range of material properties.** We measure the properties of the generated structures:  $K$  represents the bulk modulus,  $G$  denotes the shear modulus, and “Off Diagonal” refers to the sum of the upper-right  $3 \times 3$  block of  $C^H$ . Additionally,  $E_k$  indicates the Young’s modulus along the  $k$ th direction, with  $E_z$  omitted due to its close similarity to  $E_x$  and  $E_y$ . Finally, we present the UAI as  $A_U$ .

- (6) **User-specified force response.** We seek a structure with a targeted force response in a certain direction by defining  $\mathcal{E}(C^H) = |C_{kk}^H - \bar{C}_k|$ , where  $\bar{C}_k$  is a user-defined value.

$K_{\text{eff}}$ ,  $G_{\text{eff}}$ , and  $E_{\text{eff}}$  are computed in the same manner described in Sec. 5.2. The energy term  $\mathcal{E}(\cdot)$  penalizes the anisotropy of  $C^H$  by penalizing the distance to the closest isotropic elastic tensor. We initialize the optimization randomly, and employ the CMA-ES optimizer to find the optimal structures, and some of results are indicated by green stars in Figure 6.

For  $E_x$ , we achieve 72.46% of the Voigt upper bound. Using Hill’s approximation, our  $E_{\text{eff}}$  attains 58.29% of the HS bound. For  $E_{\text{eff}}$  in (2), we find an isotropic material with 54.35% of the HS bound. For  $K_{\text{eff}}$ , the optimal value is 83.36% of its theoretical upper bound. Although this is slightly lower than the best TPMS-like structures (91.83%) within our design space, it remains the highest performer at that specific volume ratio. For  $G_{\text{eff}}$ , we reach 60.79%. These outcomes closely align with the state-of-the-art results reported for the low-density range ( $V \leq 10\%$ ) in terms of Young’s modulus, bulk modulus, and shear modulus, attaining 56.57%, 94%, and 52.83%, respectively [Ma et al. 2021]. They also outperform structures with spinodal topologies, which is approximately 36.36% [Hsieh et al. 2019]. Additionally, we identify a structure with large off-diagonal entries, indicating pronounced anisotropy. All optimal results surpass those obtained

through random search, underscoring the efficacy of our approach. Finally, for the user-specified force response, we emphasize the structure’s behavior in the  $z$ -direction. By doing so, we successfully obtain structures whose  $C_{33}^H$  values are precisely 0.10, 0.20, and 0.52. These designs are then tiled into a larger block, as illustrated in the subsequent section (Figure 9).

## 5.5 Tiling and 3D printing

Our structure can be tiled because of its periodic boundaries. Moreover, different blocks can be combined to form a single larger block. Since the structure is represented by an implicit function, a smooth interpolation function can be defined at the boundaries between each pair of structures. The smooth interpolation function is defined in the Supplementary Materials. Figure 9 presents four example structures arranged into a  $5 \times 5 \times 5$  block, illustrating the feasibility of large-scale tiling.

Finally, we fabricate selected structures to demonstrate their practical use. We employ a Digital Light Processing (DLP) 3D printer to produce them in  $5 \times 5 \times 5$  blocks. Specifically, we print one structure with the highest Young’s modulus in the  $x$ -direction, another with the largest off-diagonal entries, and two tailored for a user-assigned force response. Each structure is successfully printed as a  $5 \text{ cm} \times 5 \text{ cm} \times 5 \text{ cm}$  block without support materials, taking about

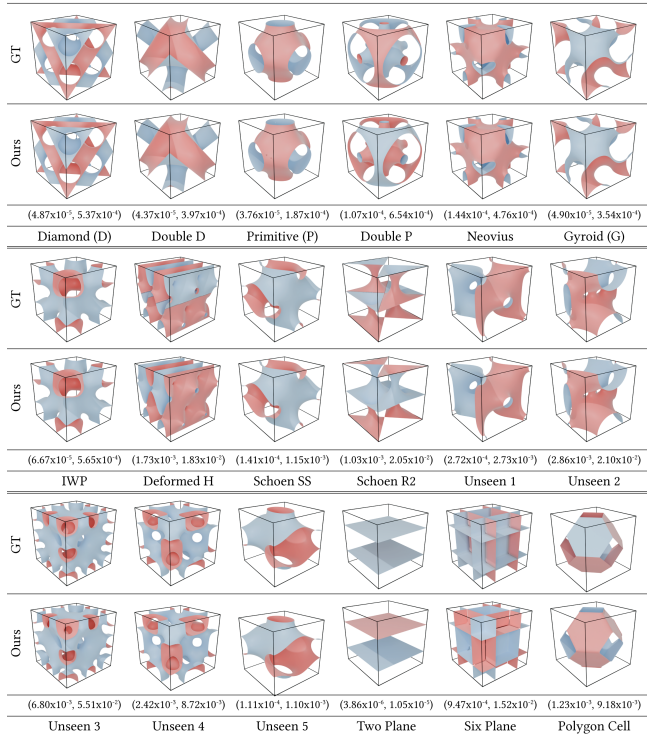


**Fig. 8. Our design space encompasses existing structures.** In particular, we show 17 TPMS and three planar structures. The small distance error above the name, represented as average distance and Hausdorff distance, underscores the accuracy of our representation.

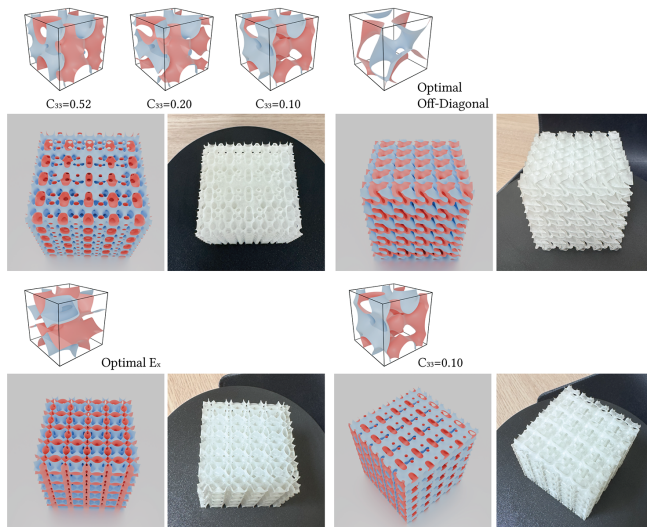


**Fig. 9. Our structures are tileable and manufacturable.** We present four distinct  $5 \times 5 \times 5$  blocks assembled from our metamaterial design. The top-left block is composed of three separate building blocks, underscoring the potential for practical usage.

one hour per structure. The wall thickness is set to 0.015 cm. The resulting structure is shown in Figure 9.

## 6 Conclusion

In this paper, we proposed a design space for shellular metamaterials that is both efficient and versatile. In addition, we developed a GPU-based method capable of rapidly generating structures defined by our design space in under 20 ms and evaluating their properties in near-real-time (under 0.5 s). We further introduce an inverse design approach that meets user requirements, such as identifying an optimal structure or producing a specific force response. Our qualitative and quantitative experiments validate the effectiveness of the proposed design space and its accompanying forward evaluation and inverse design methods. Moreover, the manufacturability of the resulting structures illustrates their strong potential for practical applications, including 3D printing infills or lightweight, high-stiffness components.

Nonetheless, since our homogenization relies on voxel-based approximations, developing a thin-shell-based simulator could potentially yield more accurate results. While our GPU-based homogenization method reduces the degrees of freedom from a cubic to a quadratic scaling with resolution, its overall performance remains slightly inferior to that of [Zhang et al. 2023]. We attribute this limitation primarily to the linear solver bottleneck. While our work has focused on mechanical applications, extending it to other areas such as fluid and thermal analysis could be promising. Finally, testing the real-world performance of these structures remains an important direction for future research.

## References

- Dirk V Arnold and Nikolaus Hansen. 2010. Active covariance matrix adaptation for the  $(1+1)$ -CMA-ES. In *Proceedings of the 12th annual conference on Genetic and evolutionary computation*. 385–392.
- Sahab Babae, Jongmin Shim, James C Weaver, Elizabeth R Chen, Nikita Patel, and Katia Bertoldi. 2013. 3D soft metamaterials with negative Poisson’s ratio. *Adv. Mater* 25, 36 (2013), 5044–5049.
- Ian Barnes et al. 1990. Microstructure of bicontinuous phases in surfactant systems. (1990).
- Katia Bertoldi, Vincenzo Vitelli, Johan Christensen, and Martin Van Hecke. 2017. Flexible mechanical metamaterials. *Nature Reviews Materials* 2, 11 (2017), 1–11.
- Antoine Chan-Lock and Miguel A Otaduy. 2024. Polar Interpolants for Thin-Shell Microstructure Homogenization. In *SIGGRAPH Asia 2024 Conference Papers*. 1–10.
- Hans A Eschenauer and Niels Olhoff. 2001. Topology optimization of continuum structures: a review. *Appl. Mech. Rev.* 54, 4 (2001), 331–390.
- Hongbin Fang, Shih-Cheng A Chu, Yutong Xia, and Kon-Well Wang. 2018. Programmable self-locking origami mechanical metamaterials. *Advanced Materials* 30, 15 (2018), 1706311.
- Marc GD Geers, Varvara G Kouznetsova, and WAM1402 Brekelmans. 2010. Multi-scale computational homogenization: Trends and challenges. *Journal of computational and applied mathematics* 234, 7 (2010), 2175–2182.
- José Miranda Guedes and Noboru Kikuchi. 1990. Preprocessing and postprocessing for materials based on the homogenization method with adaptive finite element methods. *Computer methods in applied mechanics and engineering* 83, 2 (1990), 143–198.
- Lu Han and Shunai Che. 2018. An overview of materials with triply periodic minimal surfaces and related geometry: from biological structures to self-assembled systems. *Advanced Materials* 30, 17 (2018), 1705708.
- Zvi Hashin. 1983. Analysis of composite materials—a survey. (1983).
- Zvi Hashin and Shmuel Shtrikman. 1963. A variational approach to the theory of the elastic behaviour of multiphase materials. *Journal of the Mechanics and Physics of Solids* 11, 2 (1963), 127–140.
- Richard Hill. 1952. The elastic behaviour of a crystalline aggregate. *Proceedings of the Physical Society. Section A* 65, 5 (1952), 349.
- Meng-Ting Hsieh, Bianca Endo, Yunfei Zhang, Jens Bauer, and Lorenzo Valdevit. 2019. The mechanical response of cellular materials with spinodal topologies. *Journal of*

- the Mechanics and Physics of Solids* 125 (2019), 401–419.
- Jiangbei Hu, Shengfa Wang, Baojun Li, Fengqi Li, Zhongxuan Luo, and Ligang Liu. 2020. Efficient representation and optimization for TPMS-based porous structures. *IEEE Transactions on Visualization and Computer Graphics* 28, 7 (2020), 2615–2627.
- Yu Jiang, Jiangbei Hu, Shengfa Wang, Na Lei, Zhongxuan Luo, and Ligang Liu. 2023. Meshless optimization of triply periodic minimal surface based two-fluid heat exchanger. *Computer-Aided Design* 162 (2023), 103554.
- Muamer Kadic, Tiemo Bückmann, Robert Schittny, and Martin Wegener. 2013. Metamaterials beyond electromagnetism. *Reports on Progress in physics* 76, 12 (2013), 126501.
- Sanath Keshav, Julius Herb, and Felix Fritzen. 2025. Spectral Normalization and Voigt-Reuss net: A universal approach to microstructure-property forecasting with physical guarantees. *arXiv preprint arXiv:2504.00712* (2025).
- Diederik P Kingma and Jimmy Ba. 2014. Adam: A method for stochastic optimization. *arXiv preprint arXiv:1412.6980* (2014).
- Siddhant Kumar, Stephanie Tan, Li Zheng, and Dennis M Kochmann. 2020. Inverse-designed spinodoid metamaterials. *npj Computational Materials* 6, 1 (2020), 73.
- Chenxi Lu, Mengting Hsieh, Zhifeng Huang, Chi Zhang, Yaojun Lin, Qiang Shen, Fei Chen, and Lianmeng Zhang. 2022. Architectural design and additive manufacturing of mechanical metamaterials: a review. *Engineering* 17 (2022), 44–63.
- Qingping Ma, Lei Zhang, Junhao Ding, Shuo Qu, Jin Fu, Mingdong Zhou, Ming Wang Fu, Xu Song, and Michael Yu Wang. 2021. Elastically-isotropic open-cell minimal surface shell lattices with superior stiffness via variable thickness design. *Additive Manufacturing* 47 (2021), 102293.
- Liane Makatura, Bohan Wang, Yi-Lu Chen, Bolei Deng, Chris Wojtan, Bernd Bickel, and Wojciech Matusik. 2023. Procedural metamaterials: A unified procedural graph for metamaterial design. *ACM Transactions on Graphics* 42, 5 (2023), 1–19.
- Yunwei Mao, Qi He, and Xuanhe Zhao. 2020. Designing complex architected materials with generative adversarial networks. *Science advances* 6, 17 (2020), eaaz4169.
- Ban Dang Nguyen, Jeong Shik Cho, and Kiju Kang. 2016. Optimal design of “Shellular”, a micro-architected material with ultralow density. *Materials & Design* 95 (2016), 490–500.
- NVIDIA. 2024. cuDSS. <https://docs.nvidia.com/cuda/cudss/index.html>.
- Stanley Osher, Ronald Fedkiw, Stanley Osher, and Ronald Fedkiw. 2003. Constructing signed distance functions. *Level set methods and dynamic implicit surfaces* (2003), 63–74.
- David Palmer, Dmitriy Smirnov, Stephanie Wang, Albert Chern, and Justin Solomon. 2022. Deepcurrents: Learning implicit representations of shapes with boundaries. In *Proceedings of the IEEE/CVF Conference on Computer Vision and Pattern Recognition*. 18665–18675.
- Julian Panetta, Qingnan Zhou, Luigi Malomo, Nico Pietroni, Paolo Cignoni, and Denis Zorin. 2015. Elastic textures for additive fabrication. *ACM Trans. Graph.* 34, 4 (2015), 135–1.
- Jeong Joon Park, Peter Florence, Julian Straub, Richard Newcombe, and Steven Lovegrove. 2019. DeepSDF: Learning continuous signed distance functions for shape representation. In *Proceedings of the IEEE/CVF conference on computer vision and pattern recognition*. 165–174.
- Les Piegl and Wayne Tiller. 2012. *The NURBS book*. Springer Science & Business Media.
- Michael JD Powell et al. 2009. The BOBYQA algorithm for bound constrained optimization without derivatives. *Cambridge NA Report NA2009/06, University of Cambridge, Cambridge* 26 (2009), 26–46.
- Shivakumar I Ranganathan and Martin Ostojic-Starzewski. 2008. Universal elastic anisotropy index. *Physical review letters* 101, 5 (2008), 055504.
- Sebastian Ruder. 2016. An overview of gradient descent optimization algorithms. *arXiv preprint arXiv:1609.04747* (2016).
- Christian Schumacher, Steve Marschner, Markus Gross, and Bernhard Thomaszewski. 2018. Mechanical characterization of structured sheet materials. *ACM Transactions on Graphics (TOG)* 37, 4 (2018), 1–15.
- Alessandro Spadoni, Reinhard Höhler, Sylvie Cohen-Addad, and Vladimir Dorodnitsyn. 2014. Closed-cell crystalline foams: Self-assembling, resonant metamaterials. *The Journal of the Acoustical Society of America* 135, 4 (2014), 1692–1699.
- Krister Svanberg. 2002. A class of globally convergent optimization methods based on conservative convex separable approximations. *SIAM journal on optimization* 12, 2 (2002), 555–573.
- S Torquato, S Hyun, and Aleksandar Donev. 2002. Multifunctional Composites: Optimizing Microstructures for Simultaneous Transport of Heat and Electricity. *Physical review letters* 89, 26 (2002), 266601.
- Woldemar Voigt. 1910. *Lehrbuch der kristallphysik:(mit ausschluß der kristalloptik)*. Vol. 34. BG Teubner.
- Yu Wang, Alec Jacobson, Jernej Barbič, and Ladislav Kavan. 2015. Linear subspace design for real-time shape deformation. *ACM Transactions on Graphics (TOG)* 34, 4 (2015), 1–11.
- Liang Xia and Piotr Breitkopf. 2015. Design of materials using topology optimization and energy-based homogenization approach in Matlab. *Structural and multidisciplinary optimization* 52, 6 (2015), 1229–1241.
- Rui Xu, Chuanqing Chen, Jiapeng Sun, Yulong He, Xin Li, Ming-Hui Lu, and Yanfeng Chen. 2023a. The design, manufacture and application of multistable mechanical metamaterials—a state-of-the-art review. *International Journal of Extreme Manufacturing* 5, 4 (2023), 042013.
- Yonglai Xu, Hao Pan, Ruonan Wang, Qiang Du, and Lin Lu. 2023b. New families of triply periodic minimal surface-like shell lattices. *Additive Manufacturing* 77 (2023), 103779.
- Chun Yuan, Haoyang Shi, Lei Lan, Yuxing Qiu, Cem Yuksel, Huamin Wang, Chenfanfu Jiang, Kui Wu, and Yin Yang. 2024. Volumetric Homogenization for Knitwear Simulation. *ACM Transactions on Graphics (TOG)* 43, 6 (2024), 1–19.
- Di Zhang and Ligang Liu. 2025. Asymptotic analysis and design of linear elastic shell lattice metamaterials. *ACM Transactions on Graphics (TOG)* 44, 4 (2025), 1–18.
- Di Zhang, Xiaoya Zhai, Ligang Liu, and Xiao-Ming Fu. 2023. An optimized, easy-to-use, open-source GPU solver for large-scale inverse homogenization problems. *Structural and Multidisciplinary Optimization* 66, 9 (2023), 207.

Received